In situ formation of a melt-solid interface towards stable oxygen reduction in protonic ceramic fuel cells

Desheng Feng[1], Mengran Li*[,2], Vanessa K. Peterson*[,3], Rijia Lin[1], Anita D'Angelo[4], Olexandra Marenych[5], Anya Yago[5], Bin Zulkifli Muhammad Yazid[1], Tianjiu Zhu[1], Shuai Gao[1,6], Yuming Wu[1], Zhonghua Zhu*[,1]

1. School of Chemical Engineering, The University of Queensland, Brisbane, 4072, Australia

2. Department of Chemical Engineering, the University of Melbourne, Melbourne, 3010, Australia

3. Australian Centre for Neutron Scattering, Australian Nuclear Science and Technology Organisation, Sydney, New South Wales, Australia

4. Australian Synchrotron, Australian Nuclear Science and Technology Organization, 800 Blackburn Road, Clayton, Victoria, 3168 Australia

5. Centre for Microscopy and Microanalysis, The University of Queensland, St Lucia, 4072 Australia

6. Biomass Group, College of Engineering, Nanjing Agricultural University, 40 Dianjiangtai Road, Nanjing 210031, China

Corresponding authors:

M. Li: aaron.li1@unimelb.edu.au

V.K. Peterson: vanessa.peterson@ansto.gov.au

Z. Zhu: z.zhu@uq.edu.au

Abstract

Protonic ceramic fuel cells (PCFCs) are one of the promising routes to generate power efficiently from various fuels at economically viable temperatures (500-700 °C) due to the use of fast proton conducting oxides as electrolytes. However, the power density and durability of the PCFCs are still limited by their cathodes made from solid metal oxides, which are challenging to address the sluggish oxygen reduction reaction and susceptibility to CO_2 simultaneously. Here, we report an alternative approach to address this challenge by developing a new melt-solid interface through the *in situ* alkali metal surface segregation and consecutive eutectic formation at perovskite oxide surface at PCFC operating temperatures. This new approach in cathode engineering is successfully demonstrated over a lithium and sodium co-doped $BaCo_{0.4}Fe_{0.4}Zr_{0.1}Y_{0.1}O_{3-\delta}$ perovskite as the model material. Our experimental results unveil that the unique *in situ* formed melt-solid surface stabilises the catalytically active phase in bulk and promotes catalytically active site at surface. Our novel engineered melt-solid interface enhanced the stability of the cathode against poisoning in 10% CO_2 by a factor of 1.5 in a symmetrical cell configuration and by a factor of more than two in PCFC single cells.

Keywords: Protonic ceramic fuel cell; perovskite oxide; oxygen reduction reaction; surface segregation; melt-solid interface

Introduction

Protonic ceramic fuel cells (PCFCs) with fast proton-conducting ceramics provide a promising cost-effective route for high power generation directly from a wide range of fuels (e.g. hydrogen, hydrocarbons, and ammonia) at intermediate temperatures (500 – 700 °C)[1-4]. However, the power density of PCFCs is limited by the lack of catalytically active and stable cathodes, where the oxygen reduction reaction (ORR) takes place and leads to the formation of water as the product. This unique oxygen reduction reaction at PCFCs necessitates the active cathode to be proton, oxygen, and electron (hole) conductive[5]. State-of-the-art PCFC cathodes typically have a perovskite-type structure with formula ABO_3, where the *A* site contains alkaline-earth elements such as Ba and Sr, and the *B* site contains transition metals such as Co and Fe, forming compositions such as $BaCo_{0.4}Fe_{0.4}Zr_{0.1}Y_{0.1}O_{3-\delta}$ (BCFZY)[6], $SrCo_{0.4}Fe_{0.4}Zr_{0.1}Y_{0.1}O_{3-\delta}$[7], $Sr_2Sc_{0.1}Nb_{0.1}Co_{1.5}Fe_{0.3}O_{6-\delta}$[8], and $SrCo_{0.8}Fe_{0.15}Zr_{0.05}O_{3-\delta}$[9].

Despite their mixed conductivities, most of these typical PCFC cathodes are highly susceptible to poisoning by CO_2 at PCFC operating temperatures as a result of the presence of alkaline-earth elements, which react to form carbonates, leading to irreversible loss of active cathode material. Even trace amounts of CO_2 (~ 400 ppm) in ambient air can cause rapid cathode degradation and power density loss. For example, Qi *et al*. report that 6.4 at. % Ba in BCFZY converts to $BaCO_3$ after 24 h exposure to 25 °C air with 380 ppm CO_2 [10], and Li *et al.*[11] report that 1% CO_2 in air caused a 59% activity loss by the BCFZY cathode during 120 h of PCFC operation at 700 °C. It is well known for fuel cells operated at intermediate temperatures, such as solid oxide fuel cells, that loss of cathode activity is orders of magnitude worse at reduced operating temperature as a consequence of the relatively higher stability of carbonate phases[12-14].

Common strategies to address the susceptibility of these perovskites to CO_2 rely on modification of the cathode bulk or surface to weaken the binding strength of the perovskite with CO_2 or include additional solid phases that are not CO_2 reactive. The cathode can be modified by reducing the basicity of the *A-site* cation[7,11] and/or enhancing the strength of the *B*-O bond. However, such modifications might exert a negative impact on the material's proton conductivity, which is necessary for water formation[16,17]. The inclusion of secondary phases that are not CO_2 reactive has also thus far negatively impacted ORR activity of the original cathode because the CO_2-inert phase is usually either not catalytically active or less ORR active than the primary cathode.[14,17,18] These approaches all lower the PCFC power output. Therefore, it is difficult but imperative to develop a new strategy that can realize high cathode CO_2 stability without sacrificing the ORR activity.

Herein, we pursue a new strategy to improve the CO_2 tolerance of the BCFZY material with negligible loss of ORR catalytic activity by inducing the formation of a molten-solid interface. We first introduce Li^+ and Na^+ to the BCFZY *A*-site to produce the single-phase perovskite $Ba_{0.95}(LiNa)_{0.05}Co_{0.4}Fe_{0.4}Zr_{0.1}Y_{0.1}O_{3-\delta}$ (BCFZYLN). In the presence of CO_2, the alkali metal cations in BCFZYLN co-segregate at the perovskite surface and react *in situ* with CO_2, forming a thin molten adlayer partially covering the perovskite surface. Our results show that this *in situ* developed interface effectively suppresses the carbonation of Ba in BCFZY and stabilises the ORR by re-liberating active sites and extending the active surface. Consequently, the unique melt-solid interface more than doubles the cycling stability of the PCFC single cell in CO_2 compared with the unmodified cathode. These findings point to a new strategy for the modulation of solid/liquid interfacial reactions to advance a broad range of high-temperature catalyst materials.

Results

Crystal structure and chemical composition

$BaCo_{0.4}Fe_{0.4}Zr_{0.1}Y_{0.1}O_{3-\delta}$ (BCFZY) and $Ba_{0.95}(LiNa)_{0.05}Co_{0.4}Fe_{0.4}Zr_{0.1}Y_{0.1}O_{3-\delta}$ (BCFZYLN) were synthesised *via* a typical sol-gel route. We then characterised the crystal structure of these two materials quenched from 600 °C using synchrotron X-ray powder diffraction (SXRD) and neutron powder diffraction (NPD). Diffraction data (**Fig. 1**) confirm that both BCFZY and BCFZYLN are predominantly cubic perovskites with a $Pm\bar{3}m$ space group. The higher resolution SXRD data, however, reveal that this phase contains a distribution of phases with slightly different lattice parameters, and we were able to describe the data using two phases, each with a slightly different lattice parameter, termed BCFZY-1 and -2; BCFZYLN-1 and -2 (see Supplementary Tables 1 and 2). This roughly binary distribution of phases with differing lattice parameters suggests some compositional segregation, which is consistent with that reported for other Zr-containing perovskite oxides[19,20] and ascribed to segregation between Zr and other *B*-site cations like Co and Fe[21]. Structure refinement revealed a smaller lattice constant (4.10999(4) - 4.11833(3) Å) for the Li/Na co-doped sample than the undoped material (4.11758(5) - 4.12385(5) Å), as consistent with the smaller Li^+ (0.90 Å) and Na^+ (1.16 Å) dopants relative to Ba^{2+} (1.49 Å)[22]. NPD data also reveal that the Li^+ *A* site occupancy in BCFZYLN is 2(1)% and 3.9(6)% for Na^+, which confirms that the alkali cations were doped into the perovskite lattice.

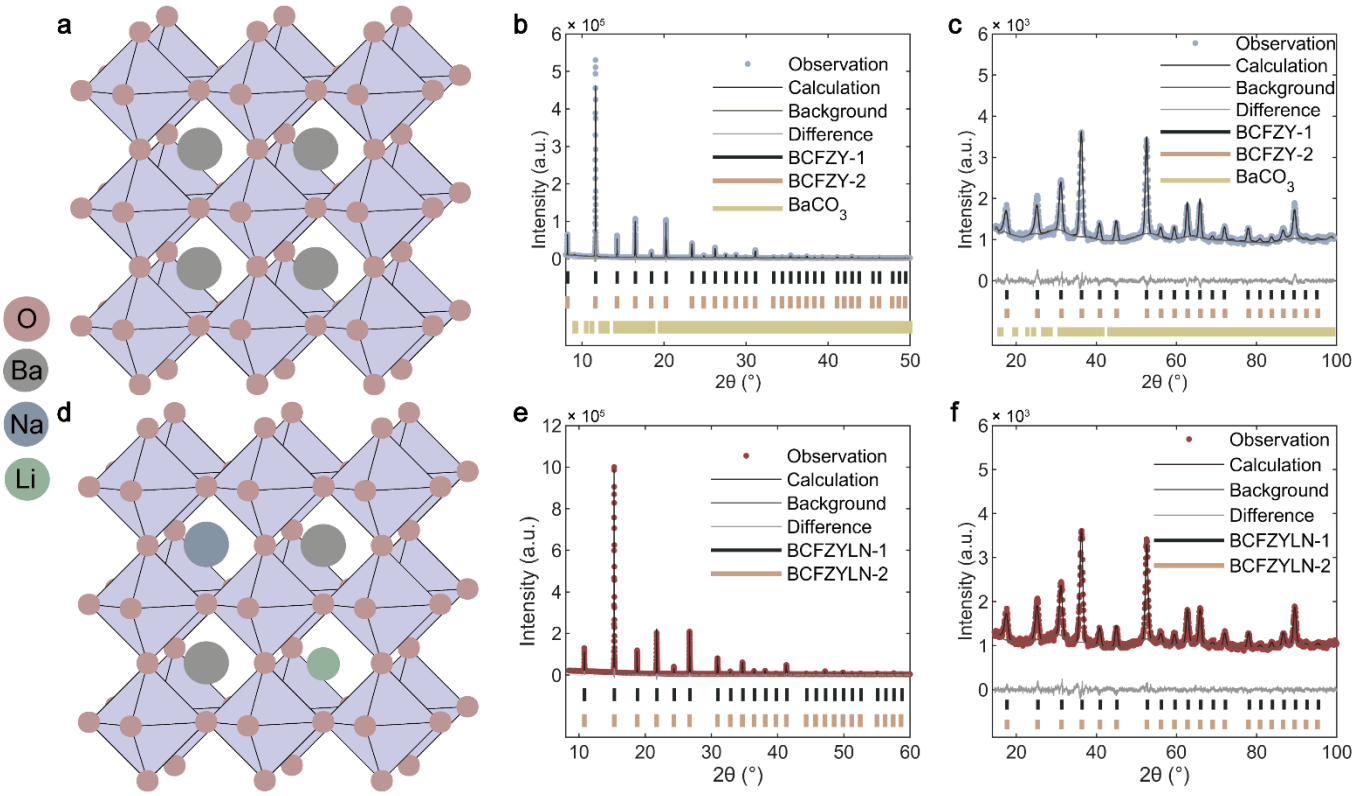

Fig. 1 BCFZY and BCFZYLN structure. a Schematic of the refined BCFZY crystal structure with *A*-site Ba^{2+} centred in the cubic perovskite structure and associated octahedra shaded. Rietveld refinement profiles using **b** SXRD and **c** NPD data of BCFZY quenched from 600 °C. **d** Schematic of the refined BCFZYLN crystal structure illustrating Li and Na *A* site doping, with the *A* site centred in the cubic perovskite structure and associated octahedra shaded. Rietveld refinement profiles using **e** SXRD and **f** NPD data of BCFZYLN quenched from 600 °C.

We then studied the chemical composition of the perovskite materials using inductively coupled plasma-optical emission spectrometry (ICP-OES). The results showed that BCFZY has an average formula of $BaCo_{0.373}Fe_{0.404}Zr_{0.122}Y_{0.102}O_{3-\delta}$, while BCFZYLN is $Ba_{0.937}Li_{0.027}Na_{0.035}Co_{0.359}Fe_{0.384}Zr_{0.099}Y_{0.158}O_{3-\delta}$, consistent with the nominal target compositions and powder diffraction data.

Oxygen non-stoichiometry, denoted as δ, quantifies oxygen vacancy in the perovskites. Supplementary Fig. 1 compares the oxygen non-stoichiometry between both samples as a function of temperature. At 600 °C, more oxygen vacancies are created in the co-doped ($\delta \sim 0.73$) than in the undoped sample ($\delta \sim 0.63$), possibly as a result of the lower valence of Li^+ and Na^+ compared with Ba^{2+}, which requires fewer O^{2-} ions to maintain the material's charge neutrality.

Cathode ORR activity and CO_2 stability

We then evaluated the ORR activity of the synthesised perovskite materials in air containing 3 vol.% moisture at 450-600 °C in symmetrical cells (**Fig. 2a**), where cathode materials are deposited onto both sides of a dense protonic conducting electrolyte disk. The ORR activity is characterised by the area-specific resistance (ASR), where a low ASR indicates a high ORR catalytic activity. The ASR is shown in **Fig. 2b** and we identify negligible differences in ORR activities between the undoped and co-doped cathode in humid air. For example, the BCFZY cathode exhibited an ASR of 0.19 ± 0.02 Ω cm^2 at 600 °C and 3.8 ± 0.2 Ω cm^2 at 450 °C, in agreement with previously reported values for the same material [6,23-25]. Similarly, BCFZYLN has an ASR of 0.20 ± 0.03 at 600 °C and 3.6 ± 0.1 Ω cm^2 at 450 °C, suggesting that Li/Na co-doping has no impact on the ORR activity of the cathode in humid air, despite the creation of additional oxygen vacancies in the structure.

We studied the CO_2 tolerance of BCFZY and BCFZYLN cathodes at 600 °C by placing the symmetrical cells in flowing humid air containing 10% CO_2 for 1 h and monitoring the time evolution of the ASR. The BCFZY cathode degrades quickly in the presence of CO_2, as evidenced by an increase in ASR from 0.19 ± 0.02 to 0.9 ± 0.1 Ω cm^2 at a rate of 7.4 ± 0.2 × 10^{-3} Ω cm^2 min^{-1} (**Fig. 2c**). Such cathode degradation is irreversible, and the ASR of the undoped cathode only recovered to 0.32 ± 0.03 Ω cm^2 following the replenishment of the test chamber with humid air free from CO_2 for 30 min. In contrast, BCFZYLN is more resistant to CO_2 poisoning than the BCFZY cathode. As shown in **Fig. 2c**, the ASR of the co-doped cathode increases from 0.20 ± 0.03 to 0.73 ± 0.08 Ω cm^2 after the same CO_2 exposure, representing a degradation rate of 4.9 ± 0.3 × 10^{-3} Ω cm^2 min^{-1}, which is ~ 33% lower than of the undoped cathode. After CO_2 removal, the co-doped cathode ASR is recovered back to 0.26 ± 0.03 Ω cm^2, ~ 20% better than that of the undoped cathode.

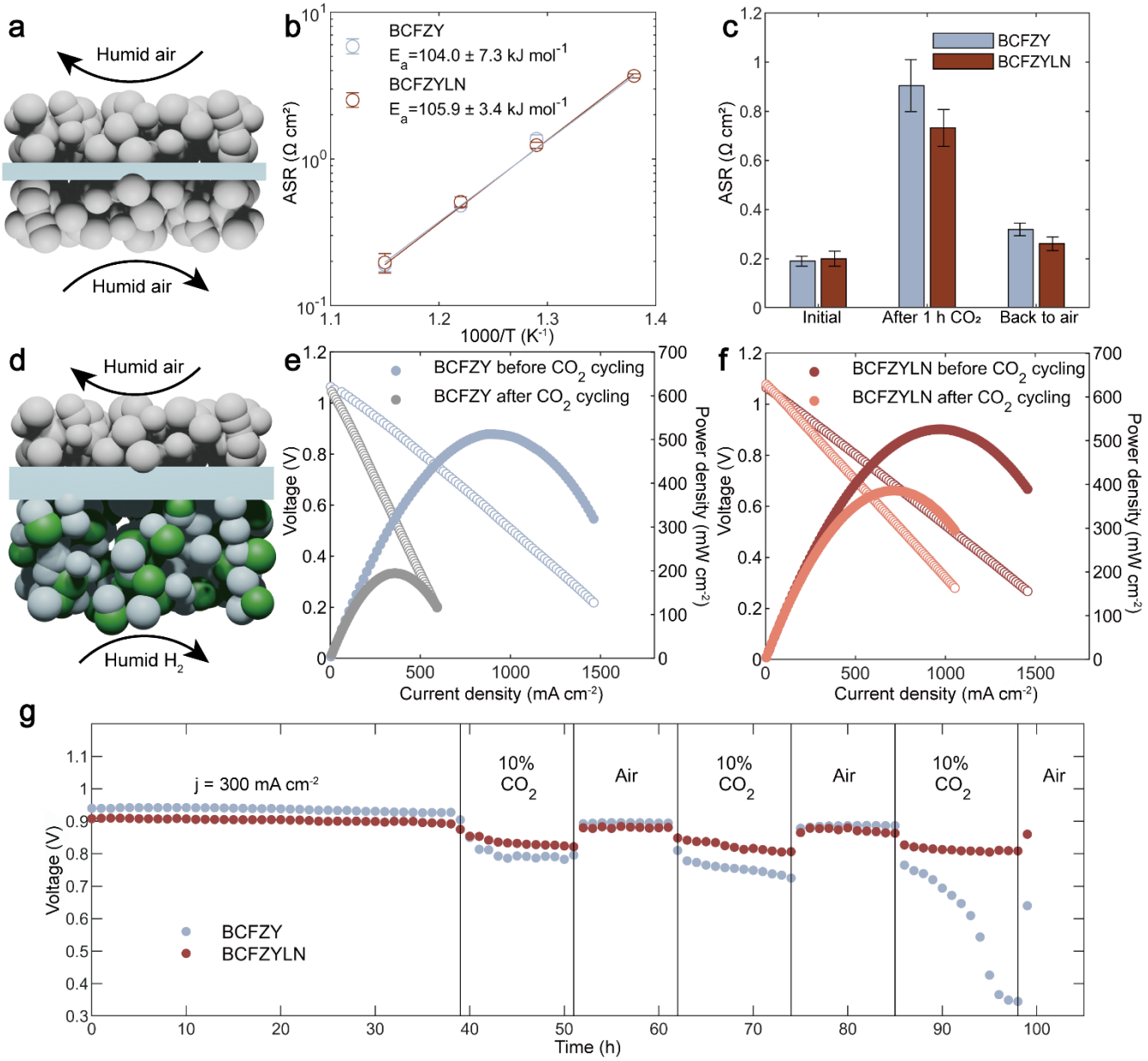

Fig. 2 ORR performance of BCFZY and BCFZYLN. a Schematic of the electrolyte-supported symmetric cell showing the dense electrolyte pellet (1% NiO + $BaZr_{0.1}Ce_{0.7}Y_{0.1}Yb_{0.1}O_{3-\delta}$ (BZCYYb) shown as a cross-section in blue) with cathode particles (spheres) coated on both sides. **b** Temperature dependence of the area-specific resistance (ASR) of BCFZY and BCFZYLN between 600 °C and 450 °C. Lines through the points are linear fits where the slope is the activation energy (E_a), as detailed inset **c** ASR of BCFZY and BCFZYLN in humid air, after exposure to 10% CO_2 for 1 h, and after 1 h re-exposure to humid air. **d** Schematic of a typical anode supported single cell, showing a dense electrolyte (BZCYYb, in blue) that separates the cathode (top) and anode (bottom) particles. Humid H_2 is supplied to the NiO-BZCYYb anode and humid air is supplied to the cathode. **e** BCFZY single cell #1 I-V-P curve before and after three cycles with CO_2 at 600 °C **f** BCFZYLN single cell #2 I-V-P curve before and after three cycles with CO_2 at 600 °C **g** Cycle stability of single-cell #1 and #2 at a current density (j) of 300 mA cm^{-2} at 600 °C.

Notably, the co-doped cathode further improves ORR activity by ~ 40% in humid air and stability by a factor of nearly five in the presence of CO_2 at 700 °C when compared with the undoped cathode. As shown in Supplementary Fig. 2, the degradation rate is 4.3 ± 0.8 × 10^{-3} Ω cm^2 min^{-1} for the undoped cathode, but only 0.9 ± 0.1 × 10^{-3} Ω cm^2 min^{-1} for the co-doped cathode. Both cathodes show better catalytic stability in CO_2 at 700 °C than at 600 °C. Such improvement is likely a consequence of the destabilised carbonate phase at elevated temperatures. In other words, a high CO_2 tolerance at reduced operating temperature is highly sought after for PCFCs that aim for low to intermediate temperature regimes.

We prepared Na and Li single-doped cathodes (termed BCFZYN and BCFZYL, see Supplementary Tables 3 and 4, respectively) and compared their CO_2 tolerance against the performance of state-of-the-art cathodes under various test conditions in Table 1. Interestingly, the co-doped cathode is superior to Li- and Na- single-doped counterparts (see Supplementary Fig. 3 and 4), implying a synergistic effect of the co-doping in resisting CO_2 poisoning. In comparison to other cathodes in Table 1, the Li/Na co-doped BCFZY is among the most active and stable cathode in humid air containing 10% CO_2 at PCFC operating temperatures.

Table 1- Comparison of CO_2 tolerance of Li/Na-doped BCFZY and reported PCFC cathodes.

Cathode	Temperature (° C)	ASR in the absence of CO_2 (Ω cm^2)	Measurement duration (h)	Degradation rate (Ω cm^2 min^{-1})	Test conditions	Reference
BCFZY	700	0.13	1	$4.3\ (8) \times 10^{-3}$	Humid air 10% CO_2	This work
	600	0.19	1	$7.4(2) \times 10^{-3}$	Humid air 10% CO_2	This work
BCFZYLN	700	0.09	1	$0.9(1) \times 10^{-3}$	Humid air 10% CO_2	This work
	600	0.21	1	$4.9(3) \times 10^{-3}$	Humid air 10% CO_2	This work
BCFZYL	600	0.23	1	$1.00(4) \times 10^{-2}$	Humid air 10% CO_2	This work
BCFZYN	600	0.23	1	$8.10(2) \times 10^{-3}$	Humid air 10% CO_2	This work
BSCF	700	-	1	4.50×10^{-2}	Humid air 10% CO_2	[9]
SCFZ	700	0.07	1	1.30×10^{-2}	Humid air 10% CO_2	[9]
SCFZY	700	0.21	1	1.10×10^{-2}	Humid air 10% CO_2	[7]
BCFZY	700	0.36	120	2.86×10^{-5}	Dry air 1% CO_2	[11]
		0.36	120	2.49×10^{-5}	Dry air 10% CO_2	[11]
BCaCFZY	700	0.29	120	8.89×10^{-6}	Dry air 1% CO_2	[11]
		0.29	120	9.17×10^{-6}	Dry air 10% CO_2	[11]
BCYF1 composite	600	0.35	2	4.00×10^{-3}	5% H_2O-air 1% CO_2	[18]
BCYF2 composite	600	0.21	2	1.00×10^{-3}	5% H_2O-air 1% CO_2	[18]
BCYF3 composite	600	0.70	2	7.13×10^{-3}	5% H_2O-air 1% CO_2	[18]
SSNCF	600	0.39	2.5	2.15×10^{-3}	Humid air 1% CO_2	[17]
3 wt% LWMN-SSNCF	600	0.32	2.5	1.33×10^{-3}	Humid air 1% CO_2	[17]
BCFCY64	600	0.67	6	1.55×10^{-3}	Humid air 10% CO_2	[26]
BCFCY73	600	0.67	6	1.55×10^{-3}	Humid air 10% CO_2	[26]
BCFCY82	600	0.67	6	1.55×10^{-3}	Humid air 10% CO_2	[26]

Note: BSCF = $Ba_{0.5}Sr_{0.5}Co_{0.8}Fe_{0.2}O_{3-\delta}$, SCFZ = $SrCo_{0.8}Fe_{0.15}Zr_{0.05}O_{3-\delta}$, SCFZY = $SrCo_{0.4}Fe_{0.4}Zr_{0.1}Y_{0.1}O_{3-\delta}$, BCaCFZY = $Ba_{0.95}Ca_{0.05}Co_{0.4}Fe_{0.4}Zr_{0.1}Y_{0.1}O_{3-\delta}$, BCYF = $Ba(Ce_{0.8}Y_{0.2})_xFe_{1-x}O_{3-\delta}$, SSNCF = $Sr_2Sc_{0.1}Nb_{0.1}Co_{1.5}Fe_{0.3}O_{6-\delta}$, LWMN = $La_{5.5}W_{0.45}Mo_{0.4}Nb_{0.15}O_{11.25-\delta}$, and BCFCY = $Ba(Co_{0.7}Fe_{0.3})_x(Ce_{0.8}Y_{0.2})_{1-x}O3_{-\delta}$.

We then compared the performance of the undoped and co-doped materials as the cathode in a single cell configuration, including stability in the presence of CO_2. A single cell is composed of a ~ 300 μm thick porous Ni-BZCYYb anode, a porous cathode, and a dense ~ 20 μm thick electrolyte separating the fuel from air (**Fig. 2d**). We fabricated two single cells with BCFZY (cell #1) and BCFZYLN (cell #2) as cathodes, with **Fig. 2e** and **f** showing the current-voltage-power (I-V-P) curves of these cells. In the absence of CO_2 at 600 °C, both cells generated similar power densities, with a peak power density of 514 mW cm^{-2} for cell #1 and 526 mW cm^{-2} for cell #2, consistent with the similar ORR catalytic activity of BCFZY and BCFZYLN in humid air.

Both cells produced relatively stable power generation under a constant current density (300 mA cm^{-2}) in the absence of CO_2 in the first 38 h. When cycling the cathode reaction environment with and without the presence of 10% CO_2 **(Fig. 2g)**, we find that cell #2, containing the co-doped cathode, outperforms cell #1 in resisting CO_2 poisoning effects during three cathode atmosphere changes. In the third cycle, in the presence of CO_2, cell #2 sustained a cell voltage above 0.8 V, more than twice that of cell #1 (< 0.4 V). Further, cell #2 regenerates a peak power density of 386 mW cm^{-2}, higher than that achieved by cell #1 (194 mW cm^{-2}), after the 3rd cycle once CO_2 was removed. These single-cell results further demonstrate the effectiveness of Li/Na co-doping to boost the stability of the cathode in the presence of CO_2.

The origin of CO_2 resistance in BCFZYLN

The role of co-doped alkali cations in suppressing carbonation

To probe the underlying mechanism behind the CO_2 tolerance enhancement achieved by Li/Na co-doping, we first collected laboratory-based X-ray powder diffraction (XRD) data of the undoped BCFZY, Li/Na co-doped, and single-doped analogues treated under flowing air containing 10% CO_2 at 600 °C for 1 h and then quenched to room temperature (Supplementary Fig. 5 with Rietveld refinement results shown in Supplementary Tables 5-8). The CO_2 treatment transformed 85.8(6)% of the BCFZY phase from a cubic perovskite structure with $Pm\bar{3}m$ symmetry to orthorhombic $BaCO_3$ with *Pmna* symmetry. $BaCO_3$ is formed from the reaction between BCFZY and CO_2 and has limited ionic- and hole-conductivities, and is primarily responsible for cathode degradation in both symmetrical and single cells in **Fig. 2**.

In contrast, co-doping of Li/Na significantly suppresses $BaCO_3$ formation, and our diffraction analyses show that the majority of the perovskite phase sustains after 1 h CO_2 exposure, with only 4.7(1)% $BaCO_3$ formed. Similarly, as shown in **Fig. 3a**, single-doping of Li or Na also limits $BaCO_3$ formation in CO_2, but not to the same extent as co-doping.

We also examined the ease of CO_2 desorption from materials by identifying the CO_2 desorption temperatures from the temperature-programmed desorption (TPD) profiles, as shown in Supplementary Fig. 6. A high CO_2 desorption temperature indicates a strong tendency for the materials to interact with CO_2. **Fig. 3d** compares the CO_2 desorption temperature of the undoped, single-doped, and co-doped samples, where the co-doped sample exhibits the weakest interaction with CO_2 and further confirms the effectiveness of co-doping to suppress CO_2 reaction.

Despite our prior work that reported the beneficial effect of single-doped alkali metals in enhancing Sr(Fe, Nb, Ta)$O_{3-\delta}$ perovskite stability against CO_2 in dry air[27], an interesting exception observed from this study is the outperformance of Li/Na co-doping in preserving the perovskite structure and destabilising the carbonate phase.

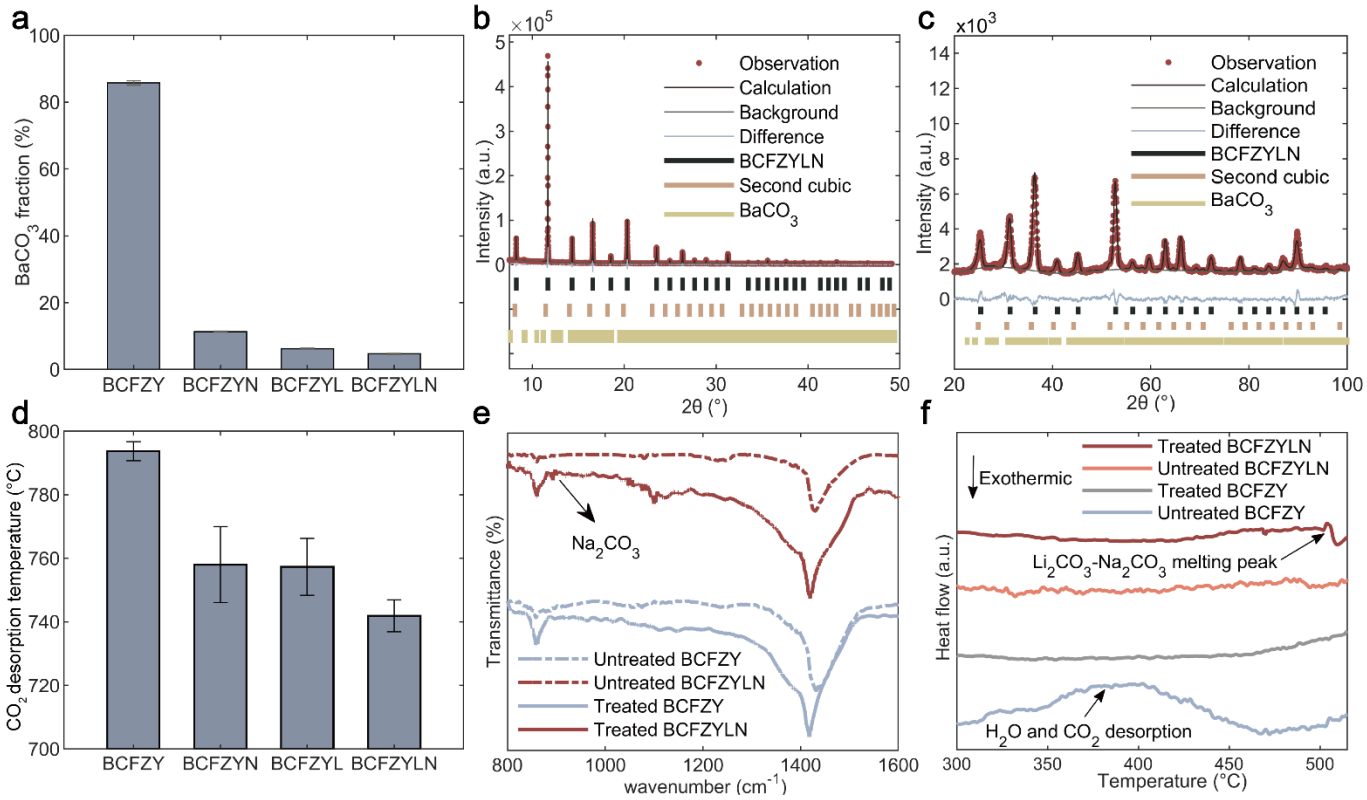

Fig. 3 Phase development and carbonate formation in the doped and pristine BCFZY cathode. a Phase % $BaCO_3$ in treated samples obtained from XRD data: BCFZY, BCFZYN, BCFZYL, and BCFZYLN = 85.8(6), 11.3(1), 6.26(1), and 4.68(1), respectively. **b** SXRD and **c** NPD refinement profiles of CO_2-treated BCFZYLN yielding 1.13(5) phase % $BaCO_3$. A second cubic phase isostructural to the main phase with $Pm\bar{3}m$ space group symmetry was identified but with a low intensity that inhibited further analysis. Full results are shown in Supplementary Table 9 and 10. **d** Temperature of the major CO_2 desorption peak. **e.** Fourier transform infrared spectra of BCFZYLN and BCFZY before and after CO_2 treatment, the feature at ~ 892 cm^{-1} is attributed to Na_2CO_3 in BCFZYLN. **f** Differential scanning calorimetry data of treated BCFZYLN and BCFZY showing an endothermic peak at ~ 500 °C for the BCFZYLN sample attributed to the melting of Li and Na carbonate.

Surface segregation of alkali dopants in the presence of CO_2

To obtain a deeper understanding of the co-doped sample's response to CO_2 conditioning, we characterised the co-doped sample using SXRD and NPD (**Fig. 3b** and **c**, and Supplementary Table 9 and 10). Results show 0(2)% Li occupancy and 0(5)% Na occupancy remaining in the BCFZYLN sample after CO_2 conditioning, less than the nominal concentration and suggesting loss of the alkali dopants from the bulk sample.

The powder diffraction result is consistent with the Li/Na carbonate species identified at the surface of CO_2-treated BCFZYLN using spectroscopic tools, with $BaCO_3$ species discernible in infrared spectra at ~ 1480 cm^{-1} and ~ 860 cm^{-1} [28] (**Fig. 3e**) and X-ray photoelectron spectroscopy (XPS) O 1*s* data at ~ 531.2 eV [29] and in C 1*s* data at ~ 289.1 eV (see Supplementary Fig. 7 and 8, respectively). The carbonate species found in the untreated undoped samples further highlight the high reactivity of the cathode surface with the trace amounts of CO_2 in air. Fourier transform infrared (FTIR) spectra of CO_2-treated BCFZYLN (**Fig. 3e**) reveal an additional adsorption infrared band at ~892 cm^{-1} [28], indicating the formation of Na_2CO_3 at the surface. However, the laboratory FTIR is unable to distinguish between Li_2CO_3 and $BaCO_3$, unlike the high-resolution XPS data (Supplementary Fig. 7 and 8) in which features at 289.6 eV and 531.7 eV are attributable to Li_2CO_3 [29,30].

These alkali metal carbonate phases are absent from the high-resolution SXRD data (**Fig. 3b**), and we postulate that the alkali metal carbonates could be amorphous. Noting that the Li_2CO_3-Na_2CO_3 binary system has a eutectic temperature of 498 °C[31,32,33], these alkali metal carbonates can be present in melts instead of crystalline solids at temperatures beyond 500 °C and form an amorphous phase while being quenched to room temperature.

Mixed alkali carbonate melt formation

Differential scanning calorimetry (DSC) measurements of the untreated and CO_2-treated cathodes were made to identify glassy transitions of the carbonate phases through changes in heat flow. **Fig. 3f** shows a broad endothermic feature in the DSC data for the untreated undoped sample at 300 - 470 °C, associated with CO_2 desorption or dehumidification processes, as observed in TPD data (Supplementary Fig. 6). Notably, we identified an endothermic feature at 504 °C only in the DSC data of the CO_2-treated BCFZYLN, consistent with the reported eutectic temperature (498 °C) for the Li_2CO_3-Na_2CO_3 binary system.[31,32,33] This feature can be a result of heat absorbed by the transition of alkali metal carbonates from amorphous to melt.

We compared the morphology of the cathode surface before and after CO_2 treatment using both scanning and transmission electron microscopy (SEM and TEM, respectively). As shown in **Fig. 4a** and **b**, an ~ 5 nm thick amorphous phase appeared in contact with the crystalline bulk of the BCFZYLN cathode but was not present at the undoped BCFZY surface after CO_2 exposure (**Fig. 4d** and **e**). Taken together with our SXRD, XPS, TPD, and DSC data, we attribute this amorphous layer in the co-doped cathode to a mixed alkali carbonate melt. SEM showed that this melt partially covers the surface of the co-doped sample (**Fig. 4c)**, which substantially differed from the surface of the treated undoped material where isolated crystalline nanoparticles, potentially of $BaCO_3$ as identified through SXRD, are visible (**Fig. 4f)**. Elemental mapping using TEM with energy dispersive spectroscopy (EDS) of these surfaces was inconclusive due to the large background signal for Na (Supplementary Fig. 10).

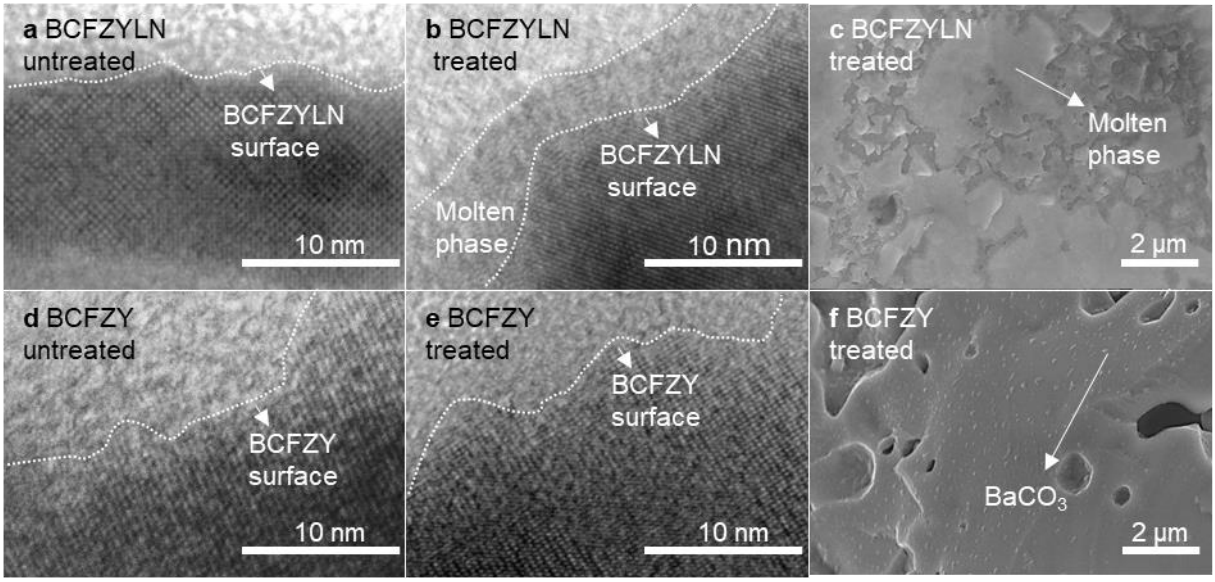

Fig. 4 Microscopy images of BCFZY and BCFZYLN before and after CO_2 treatment a Typical TEM image of untreated BCFZYLN. **b** Typical TEM image of CO_2-treated BCFZYLN revealing a phase attributed to amorphous Li_2CO_3-Na_2CO_3. **c** Typical SEM image of the amorphous Li_2CO_3-Na_2CO_3 phase in CO_2-treated BCFZYLN **d** Typical TEM image of untreated BCFZY. **e** Typical TEM image of CO_2-treated BCFZY. **f** Typical SEM image of CO_2-treated BCFZY showing a second phase attributed to $BaCO_3$.

Discussion

Our results support that co-segregation of Li/Na to the perovskite surface enables the formation of a mixed carbonate melt as identified in **Fig. 3** and **4**. Such *A*-site cation segregation is a common phenomenon in many perovskite materials at elevated temperatures,[34-40] where host/dopant cation size mismatch is widely reported as a key driving force[34,39,40] for cation surface segregation. In our material, the Shannon ionic radius is 0.92 Å for Li^+ and 1.39 Å for Na^+, much smaller than for Ba^{2+} (1.61 Å).[22] Therefore, this size mismatch likely increases the elastic energy and causes Li and Na to migrate from the bulk to the surface.

Apart from cationic size mismatch, the atmosphere also plays a role in cation segregation and melt formation. Our prior work[27] studying alkali metal single-doped $SrFeO_{3-\delta}$ perovskite oxides revealed that the presence of acidic CO_2 induces the surface segregation of basic alkali metals due to the carbonation reactions between alkali metals and CO_2. Hence, the observed co-segregation of the Li/Na surface segregation from BCFZYLN could arise from this mechanism in addition to the dopant/host size mismatch. Therefore, the segregated alkali metals make it possible for the observed formation of a Li_2CO_3-Na_2CO_3 eutectic melt adlayer *in situ* at the perovskite surface through their reaction with CO_2 at temperatures above 500 °C. Further, the low Li/Na substitutional level limits the surface availability of segregated alkali metal species, resulting in a hybrid melt-solid surface structure as shown in **Fig. 4c**, which cannot be easily achieved by other conventional techniques such as wet impregnation [41] or mechanical mixing [42]. Such a melt-solid hybrid cathode surface, as identified from this study, could be the origin of the significant improvement of CO_2 tolerance by the BCFZYLN cathode at intermediate temperatures as shown in **Fig. 2** and **Table 1**.

We envisage that the *in situ* formed melt-solid surface structure offers an opportunity to re-liberate ORR active sites and maximise surface oxygen-ion migration. In general, CO_2 deteriorates the ORR activity of perovskite oxides first through competitive adsorption at active oxygen adsorption sites. The absorbed CO_2 can further lead to the irreversible carbonation of the A-site alkaline-earth metal ions, resulting in the depletion of the catalytically active phase, as shown in **Fig. 3a**. Conventional material design strategies to address CO_2 susceptibility usually rely on either weakening the CO_2 binding strength of the material or introducing additional CO_2-insensitive solid phases[12,15,17,18]. However, both these strategies fail to counter CO_2 poisoning while sustaining a high cathodic activity under 600 °C. This limitation is because the solid surfaces resisting CO_2 adsorption or carbonation are usually compromised in oxygen adsorption, dissociation, and surface oxygen ion migration processes.

In the present work, as illustrated in **Fig. 5**, the *in situ* formed surface eutectic melt provides a pathway to transport CO_2 away from the cathode particle and also dissociate oxygen at the surface. Mixed alkali carbonate melts are known for their fast oxygen ion conduction at intermediate temperatures [43-45] and have been widely used as electrolytes in molten carbonate fuel cells [45]. Their ionic conductivities (e.g., 1.73 S m^{-1} at 600 °C for Li/Na carbonate melt) [43,44] are orders of magnitude higher than the proton/oxygen-ion conductivity of solid BCFZY (e.g., 0.16 S m^{-1} at 600 °C). The charge carriers in the carbonate melt are mobile carbonates, which undergo dynamic reactions that dissolve and release oxygen ions by absorbing and desorbing CO_2, respectively. Through this mechanism, the *in situ* formed Li/Na carbonate melt can suppress the formation of undesirable $BaCO_3$ by diverting adsorbed CO_2 away from the perovskite solid surface, re-liberating the ORR active site. The experimental results presented in **Fig. 3a-3d** confirm a much higher stability of

the alkali-metal co-doped samples in the presence of CO_2 compared to their parent oxide and Li/Na single-doped samples that do not have an alkali carbonate melt.

Further, the melt-solid interface extends the active surface for oxygen reduction and water formation across the whole cathode. Oxygen reduction is known to occur at the boundaries between the gas phase that enables oxygen supply and water vapour release, the electron-conducting phase to supply electrons, and the proton/oxygen-ion conducting phase to transport protons and produce oxygen ions.[5,8,46] In conventional solid cathodes, CO_2 mainly poisons the electron/ion-conducting phase by out-competing for oxygen vacancies and destroys the electron- and proton- conducting phases that require a stable perovskite structure and contain alkali-earth elements. When introducing melt at the surface, instead, we can reconstruct abundant CO_2-resistant active sites made from interfaces between the stable perovskite surface and the superior ion-conducting melt. In addition, the oxygen ions can be quickly transported in the surface melt to sites where protons are available for water production. In this way, the melt-solid provides a surface structure facilitating a high density of sites for combining proton and oxygen ions, which is deemed a key step to boosting the performance of protonic fuel cell cathodes.[23,25,47-49]

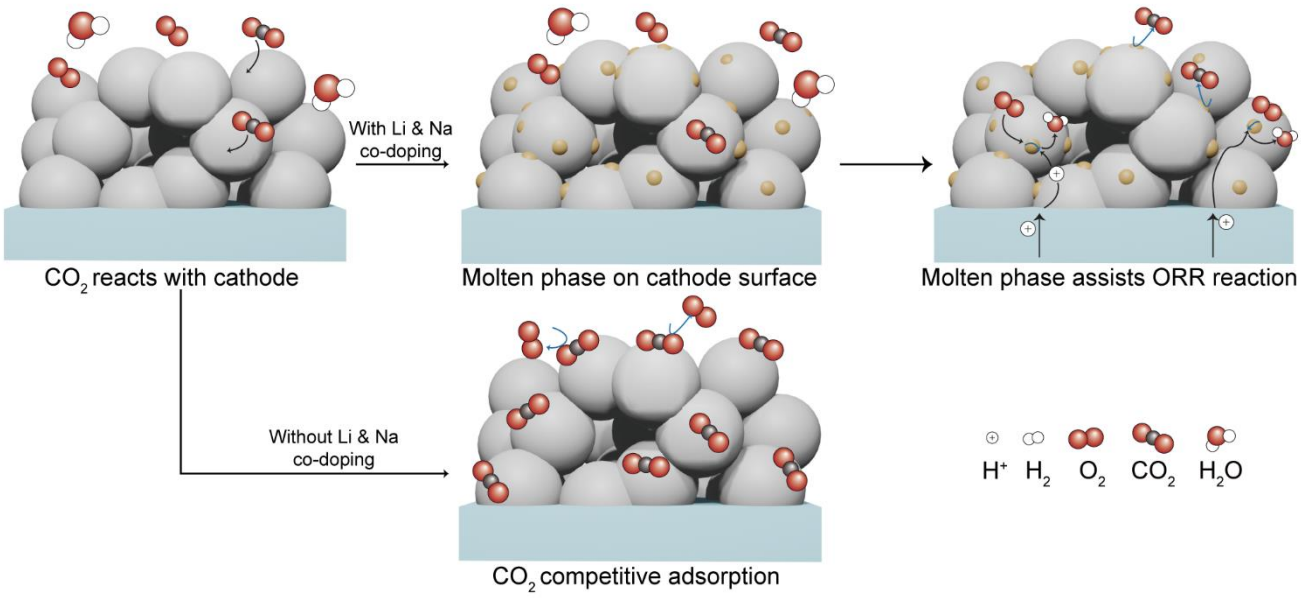

Fig. 5 Schematic of the proposed reaction mechanism of the molten-solid cathode. Above: Schematic of processes at the BCFZYLN cathode after exposure to CO_2, depicting the surface segregation of Li^+ and Na^+ which react with CO_2 to form molten-solid hybrid carbonate phases that facilitate the ORR. Below: CO_2 absorption at the surface inhibiting O_2 adsorption at the BCFZY cathode.

Conclusion

In summary, we report a cathode engineering strategy to increase the stability of the PCFC cathodes without compromising activity by developing a new melt-solid interface. By introducing Li^+ and Na^+ into the model $BaCo_{0.4}Fe_{0.4}Zr_{0.1}Y_{0.1}O_{3-\delta}$ material, we show that these alkali metal cations tend to co-segregate from bulk to the cathode surface and react with CO_2 to form a nanoscale surface layer under PCFC operating conditions. The melt-solid cathode

effectively preserves the perovskite structure and oxygen-reduction catalytic activity in the presence of CO_2. The *in situ* formed melt-perovskite interface facilitates stable and fast transport of CO_2, electrons, and ions across the cathode surface, which is important for a stable oxygen reduction reaction at practical PCFC operating conditions. This new concept in cathode design achieves significant improvement in cathode stability against 10% CO_2 in both symmetrical cell and single cell configurations. The findings of this work are expected to offer an alternative route to address the challenges in developing high-temperature solid-state electrodes by decoupling the catalytic activity and durability through *in-situ* phase segregation and solid-melt interface formation.

Acknowledgements

The authors acknowledge the facilities, and the scientific and technical assistance, of the Australian Microscopy & Microanalysis Research Facility at the Centre for Microscopy and Microanalysis, The University of Queensland. We appreciate technical support from the Australian Centre for Neutron Scattering (ACNS) for beamtime under proposal MI13525 and the Australian Synchrotron for beamtime under proposals PDR19011, PDR19087, and M19209. This work is financially supported by the Australian Research Council (ARC) DP200101397. DF acknowledges the financial support from the UQ Graduate School scholarship. ML acknowledges the financial support from ARC (DE230100637).

Methods

Sample preparation

All samples were prepared using a sol-gel method with stoichiometric salts. For example, BCFZYLN was prepared from salts of $Ba(NO_3)_2$ (99.0% Sigma-Aldrich), $Co(NO_3)_2{\cdot}6H_2O$ (99%, Sigma-Aldrich), $Fe(NO_3)_3{\cdot}9H_2O$ (98%, Sigma-Aldrich), $ZrO(NO_3)_2{\cdot}xH_2O$ (99.99% Sigma-Aldrich), $Y(NO_3)_3{\cdot}6H_2O$ (99.8%, Sigma-Aldrich), $LiNO_3$ (99.0%, Sigma-Aldrich), and $NaNO_3$ (99.0%, Sigma-Aldrich), which were dissolved in deionized water. Citric acid (99.5%, Sigma-Aldrich) was then added to the solution along with ethylenediaminetetraacetic acid (EDTA, 99.4%, Sigma-Aldrich) was first dissolved in ammonia solution (25%, Sigma-Aldrich). The molar ratio of EDTA: citric acid: total metal ions was controlled to be 3 : 3 : 2, and the final pH was increased to about 10 by adding ammonia solution.

The solution was dried using a hot plate at approximately 80 °C overnight to obtain a gel phase which was then fired at 260 °C using a fan-forced oven (Labec, general purpose 30 L) to obtain a powder. The powder was ground using an agate mortar before sintering at 1000 °C for 2 h in a horizontal tube furnace (Labec, HTFS40-300/12). The specific surface area of the as-prepared sample was determined by gas adsorption with Brunauer, Emmett and Teller (BET) theory (Supplementary Table 11) and morphology by SEM (Supplementary Fig. 9).

Powder diffraction

X-ray diffraction (XRD) data were collected at the Centre for Microscopy and Microanalysis (CMM) at the University of Queensland (UQ) using a Bruker d8 advanced diffractometer. The silicon standard reference material (SRM) 640c from the National Institute of Standards & Technology (NIST) was used to determine the instrumental parameters for the experiment using Rietveld analysis with the GSAS II software[50] and these were fixed in the subsequent structural

refinement with a starting crystal structure of $BaZr_{0.5}Fe_{0.5}O_3$ [51] and $BaCO_3$[52]. Synchrotron X-ray powder diffraction (SXRD) data were collected at the Australian Synchrotron and neutron powder diffraction (NPD) data were collected using the high-resolution powder diffractometer (Echidna)[53] at the Australian Nuclear Science and Technology Organisation (ANSTO). Samples for powder diffraction analysis were heated to 600 °C followed by air quenching. Samples were placed in glass capillaries with a diameter of 0.3 mm for SXRD data collection and in 6 mm diameter vanadium cans for NPD data collection and data collected under ambient conditions. The $La^{11}B_6$ SRM 660b from the National Institute of Standards & Technology (NIST) was used to determine the wavelength and instrumental parameters for the SXRD and NPD experiments using Rietveld analysis with the GSAS II software [50] (see Supplementary Fig. 12 and 13, respectively), and these were fixed in the subsequent structural refinement with a starting crystal structure of $BaZr_{0.5}Fe_{0.5}O_3$ [51] and $BaCO_3$ [52]. In SXRD refinements, Fe and Co are considered identical because of their similar atomic number. In both SXRD and NPD refinements, Zr and Y are considered identical because of their similar atomic number and neutron scattering length [54]. In our refinement, the ICP-OES results were used to determine some atomic occupancies.A second perovskite with a different lattice parameter (~ 4.21 Å) was identified in our SXRD data, and included in the refinement using the NPD data, with the weight fraction fixed to that obtained in the SXRD refinement. Similar phase segregation was also reported in other Zr-containing perovskite oxides, such as $BaCo_{0.4}Fe_{0.4}Zr_{0.2}O_{3-\delta}$[19] and $SrCo_{0.4}Fe_{0.6-x}Zr_xO_{3-\delta}$[20], which are attributed to the segregation between Zr and other *B*-site cations like Co and Fe [21].

ICP-OES

Powder samples were first dissolved at 200 °C with at 9:3:2 ratio of HNO_3, HF and HCl acids by microwave. 20 mL 5% boric acid was then added to neutralise the unreated HF acid. The solution was then analysed on a Thermo ICAP PRO XP ICP-OES instrument.

Phase analysis post CO_2 reaction

To investigate the phases in sample reacted with CO_2, approximately 0.1 g of samples were treated in humid air containing 10% CO_2 for 1 h at 600 °C in a horizontal tube furnace. After treatment, the sample was quenched to room temperature in air and investigated using laboratory based XRD, SXRD, and NPD, as outlined above.

Thermogravimetric analysis (TGA)

Material weight loss was investigated in air over the temperature range 200 – 700 °C using a thermogravimetric analysis system (Perkin Elmer STA 6000). Samples were first calcined at 200 °C in dry air for 1 h to remove absorbed moisture before heating to 700 °C at a ramp rate of 2 °C min^{-1}.

Oxygen non-stoichiometry analysis using titration

A sodium thiosulfate solution (0.05 M) was first prepared by dissolving $Na_2S_2O_3$ (99.99%, Sigma Aldrich) in pure water (Milli-Q Type 1 Ultrapure Water System). A small amount of sodium bicarbonate was added to the solution to maintain a basic solution in which to stabilise $Na_2S_2O_3$. 0.05 g sample was dissolved in ~ 10 mL 2 M HCl (Sigma Aldrich) and deionized water was added to dilute to ~ 200 mL. Excess KI (99.0%, Sigma Aldrich) was added to the dilute solution

to reduce transition metals. Approximately 2 mL of starch solution (Sigma Aldrich) was then added as the indicator and the solution was titrated with sodium thiosulfate solution.

Temperature-programmed desorption (TPD)

CO_2-TPD was performed using BETCAT and BETMASS systems. Approximately 0.1 g of powder was first treated in humid CO_2 at 600 °C for 1 h followed by quenching to room temperature. The as-treated sample was placed in a U-shaped tube for TPD analysis. Samples were first heated to and held at 200 °C for 1 h to remove moisture, before heating to 800 °C at 2 °C min^{-1} under Ar flow. The gas desorbed during this period was sampled and analysed by the bel-mass system.

Fourier-transform infrared (FTIR) spectroscopy

Powders were first mixed with KBr (Sigma-Aldrich, 99.9%) for dilution. FTIR spectra were measured using a Spectrum 100, PerkinElmer, in the frequency range 800-2,000 cm^{-1} in attenuated total reflection mode. The resolution was 2 cm^{-1} and each sample was scanned for 4 times.

X-ray photoelectron spectroscopy (XPS)

XPS data were measured using a Kratos Axis Ultra spectrometric in the University of Queensland's CMM with an Al Kα (1,486.8 eV) radiation source at 150 W. Fine scans were used to obtain O1s and C1s spectra and data were analysed using the CasaII software. The adventitious carbon was used for XPS calibration.

Electron microscopy

Samples for scanning electrom microscopy (SEM) analysis were pelletized and sintered at 1200 °C for 5 h to obtain dense pellets. The dense pellets (~ 0.3 g) were treated in 10% CO_2 at 600 °C for 1 h followed by quenching. The quenched samples were cracked and mounted for SEM. SEM data were obtained using a JEOL JSM-7001F at the University of Queensland's CMM operating at 20 kV. Samples for transmission electron microscopy (TEM) analysis were ground and sized using a 100 μm sieve. The powder samples were treated in 10% CO_2 at 600 °C for 1 h and were quenched to room temperature, The quenched samples were dispersed in ethanol by ultrasonic water baths. TEM images were acquired using the Hitachi HT7700 equipped with a LaB6 filament at 120kV and the TEM Energy-dispersive X-ray spectroscopy (EDS) mapping was done using Bruker EDS system for elemental analysis at the Centre for Microscopy and Microanalysis (CMM), The University of Queensland.

Differential scanning calorimetry (DSC)

DSC curves were obtained using a NETZSCH Photo-DSC 204 F1 Phoenix differential scanning calorimeter at the University of Queensland's CMM. Phase pure samples and CO_2-treated samples were placed in Al cans and heated to 520 °C, with the heat flow compared to an empty Al can.

Symmetric cell preparation

Approximately 5 g of powder cathode was mixed with 50 mL iso-propanol (99.5%, Sigma-Aldrich) and 3 mL of glycerol (99.0%, Sigma-Aldrich) and ball milled for 2 h in a planetary ball mill (Fritsch Pulverisette 5). The slurry was then

coated onto an electrolyte surface by spray coating using a conventional spray gun. The thickness of the cathode layer was controlled to be ~ 10 μm by controlling the time of coating. After coating, the cell was sintered at 900 °C for 2 h in a horizontal tube furnace (Labec, HTFS40-300/12) to obtain cells with a cathode|electrolyte|cathode configuration.

Electrochemical impedance spectroscopy (EIS)

The as-prepared symmetrical cells were heated in a horizontal tube furnace (Labec, HTFS40-300/120). Air was humidified via a wash bottle before being supplied to the cell. The airflow rate was approximately 200 mL min^{-1}. An Autolab PGSTAT30 instrument was used to perform EIS tests in the frequency range 10^5 to 10^{-1} Hz with a 10 mV amplitude. Post EIS test cells were also heated to 600 °C and exposed to 10% CO_2 where further EIS was performed every 5 min for a 1 h period. After 1 h 10% CO_2 exposure, 200 mL min^{-1} fresh humid air was supplied to the cells for 1 h and EIS measurements again performed.

Single cell fabrication

Single cells were fabricated using a solid-state reaction method. Taking the anode supporting layer (NiO : BZCYYb : starch = 6 : 4 : 1) as an example, raw materials were mixed and ball-milled in ethanol to obtain a homogeneous powder. The powder was then pressed to form the anode support layer. The electrolyte (BZCYYb + 1% NiO) was obtained using a similar method and coated on the anode by co-pressing. The anode and electrolyte half cell were then sintered at 1350 °C for 7 h to densify the electrolyte layer. The cathode was coated on the electrolyte surface by spray coating followed by sintering at 950 °C for 2 h.

Reference

1 Fabbri, E., Bi, L., Pergolesi, D. & Traversa, E. Towards the Next Generation of Solid Oxide Fuel Cells Operating Below 600 °C with Chemically Stable Proton-Conducting Electrolytes. *Advanced Materials* **24**, 195-208, doi:https://doi.org/10.1002/adma.201103102 (2012).

2 Bian, W. *et al.* Revitalizing interface in protonic ceramic cells by acid etch. *Nature* **604**, 479-485, doi:10.1038/s41586-022-04457-y (2022).

3 Wang, Z. *et al.* Rational design of perovskite ferrites as high-performance proton-conducting fuel cell cathodes. *Nature Catalysis* **5**, 777-787, doi:10.1038/s41929-022-00829-9 (2022).

4 Yang, L. *et al.* Enhanced Sulfur and Coking Tolerance of a Mixed Ion Conductor for SOFCs: BaZr0.1Ce0.7Y0.2–xYbxO3–δ. *Science* **326**, 126-129, doi:10.1126/science.1174811 (2009).

5 Kim, J. *et al.* Triple-Conducting Layered Perovskites as Cathode Materials for Proton-Conducting Solid Oxide Fuel Cells. *ChemSusChem* **7**, 2811-2815, doi:https://doi.org/10.1002/cssc.201402351 (2014).

6 Duan, C. *et al.* Readily processed protonic ceramic fuel cells with high performance at low temperatures. *Science* **349**, 1321-1326, doi:10.1126/science.aab3987 (2015).

7 Lv, X. *et al.* SrCo0.4Fe0.4Zr0.1Y0.1O3-δ, A new CO2 tolerant cathode for proton-conducting solid oxide fuel cells. *Renewable Energy* **185**, 8-16, doi:https://doi.org/10.1016/j.renene.2021.12.030 (2022).

8 Zhou, C. *et al.* New reduced-temperature ceramic fuel cells with dual-ion conducting electrolyte and triple-conducting double perovskite cathode. *Journal of Materials Chemistry A* **7**, 13265-13274, doi:10.1039/C9TA03501J (2019).

9 Lv, X., Chen, H., Zhou, W., Li, S.-D. & Shao, Z. A CO2-tolerant SrCo0.8Fe0.15Zr0.05O3−δ cathode for proton-conducting solid oxide fuel cells. *Journal of Materials Chemistry A* **8**, 11292-11301, doi:10.1039/D0TA02435J (2020).

10 Qi, H., Zhao, Z., Tu, B. & Cheng, M. Reaction tuned formation of hierarchical BaCo0.4Fe0.4Zr0.1Y0.1O3-δ cathode. *Journal of Power Sources* **455**, 227971, doi:https://doi.org/10.1016/j.jpowsour.2020.227971 (2020).
11 Li, J. *et al.* Ca-containing Ba0·95Ca0·05Co0·4Fe0·4Zr0·1Y0·1O3-δ cathode with high CO2-poisoning tolerance for proton-conducting solid oxide fuel cells. *Journal of Power Sources* **453**, 227909, doi:https://doi.org/10.1016/j.jpowsour.2020.227909 (2020).
12 Zhang, Y. *et al.* Evaluation of the CO2 Poisoning Effect on a Highly Active Cathode SrSc0.175Nb0.025Co0.8O3-δ in the Oxygen Reduction Reaction. *ACS Applied Materials & Interfaces* **8**, 3003-3011, doi:10.1021/acsami.5b09780 (2016).
13 Zhou, W., Liang, F., Shao, Z. & Zhu, Z. Hierarchical CO2-protective shell for highly efficient oxygen reduction reaction. *Scientific Reports* **2**, 327, doi:10.1038/srep00327 (2012).
14 Li, M., Zhou, W. & Zhu, Z. Highly CO2-Tolerant Cathode for Intermediate-Temperature Solid Oxide Fuel Cells: Samarium-Doped Ceria-Protected SrCo0.85Ta0.15O3−δ Hybrid. *ACS Applied Materials & Interfaces* **9**, 2326-2333, doi:10.1021/acsami.6b12606 (2017).
15 Shin, J. F. *et al.* Self-assembled dynamic perovskite composite cathodes for intermediate temperature solid oxide fuel cells. *Nature Energy* **2**, 16214, doi:10.1038/nenergy.2016.214 (2017).
16 Papac, M., Stevanović, V., Zakutayev, A. & O'Hayre, R. Triple ionic–electronic conducting oxides for next-generation electrochemical devices. *Nature Materials* **20**, 301-313, doi:10.1038/s41563-020-00854-8 (2021).
17 Wang, X. *et al.* Enhanced proton conductivity and CO2-tolerance of intermediate-temperature protonic ceramic fuel cell with lanthanum tungstate-based composite cathode. *Composites Part B: Engineering* **253**, 110565, doi:https://doi.org/10.1016/j.compositesb.2023.110565 (2023).
18 Zou, D. *et al.* The BaCe0.16Y0.04Fe0.8O3−δ nanocomposite: a new high-performance cobalt-free triple-conducting cathode for protonic ceramic fuel cells operating at reduced temperatures. *Journal of Materials Chemistry A* **10**, 5381-5390, doi:10.1039/D1TA10652J (2022).
19 Efimov, K., Czuprat, O. & Feldhoff, A. In-situ X-ray diffraction study of carbonate formation and decomposition in perovskite-type BCFZ. *Journal of Solid State Chemistry* **184**, 1085-1089, doi:https://doi.org/10.1016/j.jssc.2011.03.023 (2011).
20 Yang, L. *et al.* A New Series of Sr(Co,Fe,Zr)O3-δ Perovskite-Type Membrane Materials for Oxygen Permeation. *Industrial & Engineering Chemistry Research* **42**, 2299-2305, doi:10.1021/ie020931e (2003).
21 Kim, J. H. *et al.* Self-assembled nano-composite perovskites as highly efficient and robust hybrid cathodes for solid oxide fuel cells. *Journal of Materials Chemistry A* **10**, 2496-2508, doi:10.1039/D1TA08178K (2022).
22 Shannon, R. D. Revised effective ionic radii and systematic studies of interatomic distances in halides and chalcogenides. *Acta Cryst. A* **32**, 751-767, doi:10.1107/S0567739476001551 (1976).
23 Song, Y. *et al.* Self-Assembled Triple-Conducting Nanocomposite as a Superior Protonic Ceramic Fuel Cell Cathode. *Joule* **3**, 2842-2853, doi:https://doi.org/10.1016/j.joule.2019.07.004 (2019).
24 Liang, M. *et al.* Nickel-doped BaCo0.4Fe0.4Zr0.1Y0.1O3-δ as a new high-performance cathode for both oxygen-ion and proton conducting fuel cells. *Chemical Engineering Journal* **420**, 127717, doi:https://doi.org/10.1016/j.cej.2020.127717 (2021).
25 Liang, M. *et al.* A New Durable Surface Nanoparticles-Modified Perovskite Cathode for Protonic Ceramic Fuel Cells from Selective Cation Exsolution under Oxidizing Atmosphere. *Advanced Materials* **34**, 2106379, doi:https://doi.org/10.1002/adma.202106379 (2022).
26 Xie, C. *et al.* Investigation of Self-Assembled Dual-Phase Cathodes with Triple Conductivity for Protonic Ceramic Fuel Cells. *ACS Applied Energy Materials* **6**, 5979-5988, doi:10.1021/acsaem.3c00439 (2023).
27 Rehman, A. U. *et al.* Enhancing Oxygen Reduction Reaction Activity and CO2 Tolerance of Cathode for Low-Temperature Solid Oxide Fuel Cells by in Situ Formation of Carbonates. *ACS Applied Materials & Interfaces* **11**, 26909-26919, doi:10.1021/acsami.9b07668 (2019).
28 Linstrom, P. J. & Mallard, W. G. The NIST Chemistry WebBook: A Chemical Data Resource on the Internet. *Journal of Chemical & Engineering Data* **46**, 1059-1063, doi:10.1021/je000236i (2001).
29 Cedric, P. NIST Data Resources for X-Ray Photoelectron Spectroscopy. (2000).
30 Shchukarev, A. V. & Korolkov, D. V. XPS Study of group IA carbonates. *Central European Journal of Chemistry* **2**, 347-362, doi:10.2478/BF02475578 (2004).
31 Eitel, W. & Skaliks, W. Über einige Doppelcarbonate der Alkalien und Erdalkalien. *Zeitschrift für anorganische und allgemeine Chemie* **183**, 263-286, doi:https://doi.org/10.1002/zaac.19291830119 (1929).

32 Jiang, Y., Sun, Y., Bruno, F. & Li, S. Thermal stability of Na2CO3-Li2CO3 as a high temperature phase change material for thermal energy storage. *Thermochimica Acta* **650**, 88-94, doi:https://doi.org/10.1016/j.tca.2017.01.002 (2017).

33 Lv, W., Tong, Z., Yin, Y.-M., Yin, J. & Ma, Z.-F. Novel Nano-composites SDC–LiNaSO4 as Functional Layer for ITSOFC. *Nano-Micro Letters* **7**, 268-275, doi:10.1007/s40820-015-0038-4 (2015).

34 Lee, W., Han, J. W., Chen, Y., Cai, Z. & Yildiz, B. Cation Size Mismatch and Charge Interactions Drive Dopant Segregation at the Surfaces of Manganite Perovskites. *Journal of the American Chemical Society* **135**, 7909-7925, doi:10.1021/ja3125349 (2013).

35 Meyer, R., Waser, R., Helmbold, J. & Borchardt, G. Cationic Surface Segregation in Donor-Doped SrTiO3 Under Oxidizing Conditions. *Journal of Electroceramics* **9**, 101-110, doi:10.1023/A:1022898104375 (2002).

36 Huber, A.-K. *et al.* In situ study of activation and de-activation of LSM fuel cell cathodes – Electrochemistry and surface analysis of thin-film electrodes. *Journal of Catalysis* **294**, 79-88, doi:https://doi.org/10.1016/j.jcat.2012.07.010 (2012).

37 Rupp, G. M. *et al.* Surface chemistry of La0.6Sr0.4CoO3−δ thin films and its impact on the oxygen surface exchange resistance. *Journal of Materials Chemistry A* **3**, 22759-22769, doi:10.1039/C5TA05279C (2015).

38 Veen, A. C. v., Rebeilleau, M., Farrusseng, D. & Mirodatos, C. Studies on the performance stability of mixed conducting BSCFO membranes in medium temperature oxygen permeation. *Chemical Communications*, 32-33, doi:10.1039/B207848A (2003).

39 Cai, Z., Kuru, Y., Han, J. W., Chen, Y. & Yildiz, B. Surface Electronic Structure Transitions at High Temperature on Perovskite Oxides: The Case of Strained La0.8Sr0.2CoO3 Thin Films. *Journal of the American Chemical Society* **133**, 17696-17704, doi:10.1021/ja2059445 (2011).

40 Koo, B. *et al.* Enhanced oxygen exchange of perovskite oxide surfaces through strain-driven chemical stabilization. *Energy & Environmental Science* **11**, 71-77, doi:10.1039/C7EE00770A (2018).

41 Saqib, M. *et al.* Modification of Oxygen-Ionic Transport Barrier of BaCo0.4Zr0.1Fe0.4Y0.1O3 Steam (Air) Electrode by Impregnating Samarium-Doped Ceria Nanoparticles for Proton-Conducting Reversible Solid Oxide Cells. *Journal of The Electrochemical Society* **166**, F746, doi:10.1149/2.0461912jes (2019).

42 Lin, B. *et al.* Intermediate-to-low temperature protonic ceramic membrane fuel cells with Ba0.5Sr0.5Co0.8Fe0.2O3-δ–BaZr0.1Ce0.7Y0.2O3-δ composite cathode. *Journal of Power Sources* **186**, 58-61, doi:https://doi.org/10.1016/j.jpowsour.2008.09.041 (2009).

43 Kojima, T., Miyazaki, Y., Nomura, K. & Tanimoto, K. Electrical conductivity of molten Li2CO3-X2CO3 (X : Na, K, Rb, and Cs) and Na2CO3-Z(2)CO(3) (Z : K, Rb, and Cs). *Journal of the Electrochemical Society* **154**, F222-F230, doi:10.1149/1.2789389 (2007).

44 Zhadan, A. *et al.* Transport properties in molten carbonates: self-diffusion and conductivity measurements at high temperature. *International Journal of Hydrogen Energy* **46**, 15059-15065, doi:https://doi.org/10.1016/j.ijhydene.2020.06.294 (2021).

45 Ang, P. G. P. & Sammells, A. F. Influence of Electrolyte Composition on Electrode Kinetics in the Molten Carbonate Fuel Cell. *Journal of The Electrochemical Society* **127**, 1287, doi:10.1149/1.2129873 (1980).

46 Fabbri, E., Pergolesi, D. & Traversa, E. Materials challenges toward proton-conducting oxide fuel cells: a critical review. *Chemical Society Reviews* **39**, 4355-4369, doi:10.1039/B902343G (2010).

47 Duan, C., Huang, J., Sullivan, N. & O'Hayre, R. Proton-conducting oxides for energy conversion and storage. *Applied Physics Reviews* **7**, 011314, doi:10.1063/1.5135319 (2020).

48 Kim, J. H. *et al.* Water as a hole-predatory instrument to create metal nanoparticles on triple-conducting oxides. *Energy & Environmental Science* **15**, 1097-1105, doi:10.1039/D1EE03046A (2022).

49 Pei, K. *et al.* Surface restructuring of a perovskite-type air electrode for reversible protonic ceramic electrochemical cells. *Nature Communications* **13**, 2207, doi:10.1038/s41467-022-29866-5 (2022).

50 Toby, B. H. & Von Dreele, R. B. GSAS-II: the genesis of a modern open-source all purpose crystallography software package. *Journal of Applied Crystallography* **46**, 544-549, doi:doi:10.1107/S0021889813003531 (2013).

51 BaZr1−xFexO3, x= 0.50 (BaZr0.5Fe0.5O3) Crystal Structure: Datasheet from "PAULING FILE Multinaries Edition – 2022" in SpringerMaterials (https://materials.springer.com/isp/crystallographic/docs/sd_1244272) (Springer-Verlag Berlin Heidelberg & Material Phases Data System (MPDS), Switzerland & National Institute for Materials Science (NIMS), Japan).

52 BaCO3 (Ba[CO3] rt) Crystal Structure: Datasheet from "PAULING FILE Multinaries Edition – 2022" in SpringerMaterials (https://materials.springer.com/isp/crystallographic/docs/sd_0310722) (Springer-Verlag Berlin Heidelberg & Material Phases Data System (MPDS), Switzerland & National Institute for Materials Science (NIMS), Japan).

53 Avdeev, M. & Hester, J. R. ECHIDNA: a decade of high-resolution neutron powder diffraction at OPAL. *Journal of Applied Crystallography* **51**, 1597-1604, doi:doi:10.1107/S1600576718014048 (2018).

54 Sears, V. F. Neutron scattering lengths and cross sections. *Neutron News* **3**, 26-37, doi:10.1080/10448639208218770 (1992).